

Infrared-Assisted Single-Stage Framework for Joint Restoration and Fusion of Visible and Infrared Images under Hazy Conditions

Huafeng Li, Jiaqi Fang, Yafei Zhang, Yu Liu, Zhengtao Yu

Abstract—Infrared and visible (IR-VIS) image fusion has gained significant attention for its broad application value. However, existing methods often neglect the complementary role of infrared image in restoring visible image features under hazy conditions. To address this, we propose a joint learning framework that utilizes infrared image for the restoration and fusion of hazy IR-VIS images. To mitigate the adverse effects of feature diversity between IR-VIS images, we introduce a prompt generation mechanism that regulates modality-specific feature incompatibility. This creates a prompt selection matrix from non-shared image information, followed by prompt embeddings generated from a prompt pool. These embeddings help generate candidate features for dehazing. We further design an infrared-assisted feature restoration mechanism that selects candidate features based on haze density, enabling simultaneous restoration and fusion within a single-stage framework. To enhance fusion quality, we construct a multi-stage prompt embedding fusion module that leverages feature supplementation from the prompt generation module. Our method effectively fuses IR-VIS images while removing haze, yielding clear, haze-free fusion results. In contrast to two-stage methods that dehaze and then fuse, our approach enables collaborative training in a single-stage framework, making the model relatively lightweight and suitable for practical deployment. Experimental results validate its effectiveness and demonstrate advantages over existing methods. The source code of the paper is available at <https://github.com/fangjiaqi0909/IASSF>.

Index Terms—IR-VIS Image Fusion, Haze Removal, Joint Restoration and Fusion.

I. INTRODUCTION

Infrared and visible (IR-VIS) image fusion effectively combines the unique information from both infrared and visible images, creating a composite image that integrates their complementary features. This fused image not only provides a comprehensive and accurate scene representation but also significantly aids observers in understanding and analyzing complex environments. Consequently, this technology holds tremendous potential and value in fields such as military recon-

This work was supported in part by the National Natural Science Foundation of China under Grants (62161015, 62276120), and in part by the Yunnan Fundamental Research Projects under Grants (202301AV070004, 202401AS070640).

H. Li, J. Fang, Y. Zhang and Z. Yu are with the Faculty of Information Engineering and Automation, Kunming University of Science and Technology, Kunming 650500, China. (E-mail: lhchina99@kust.edu.cn (H. Li); fangjiaqi0909@outlook.com (J. Fang); zyfeimail@163.com (Y. Zhang); ztyu@hotmail.com (Z. Yu))

Y. Liu is with The School of Instrument Science and Opto-Electronic Engineering, Hefei University of Technology, Hefei 230009, China. (E-mail: yuliu@hfut.edu.cn)

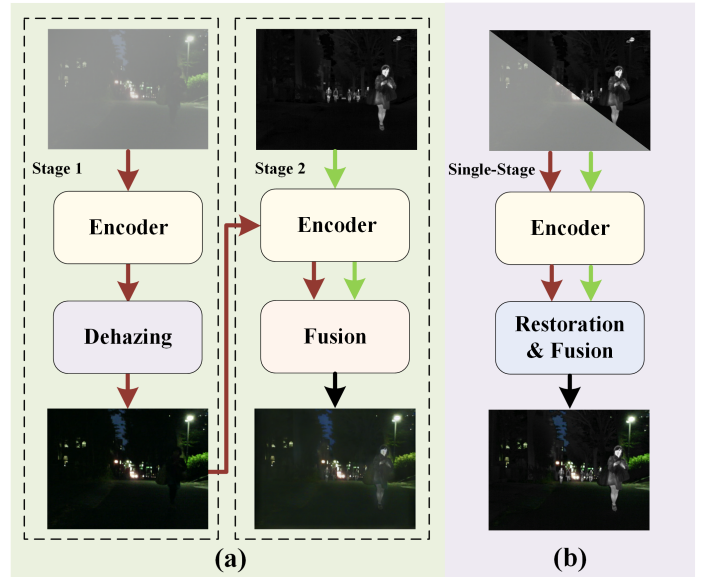


Fig. 1. Comparison of existing method and our method for hazy IR-VIS image fusion. (a) The existing method, (b) Our method.

naissance, aerospace, environmental monitoring, and medical diagnostics.

In recent years, significant progress has been made in IR-VIS image fusion [1]–[5]; however, existing methods generally assume that the input visible images are of good visual quality. In hazy conditions, visible images are affected by haze, resulting in unclear imagery, which makes it difficult for these methods to generate clear, haze-free fusion results. Traditional approaches typically address this issue by first applying a dehazing algorithm to the hazy image and then fusing the dehazed image with the infrared image, as shown in Fig. 1(a). Although this two-stage strategy is feasible, it fails to integrate the dehazing and fusion tasks into a unified framework for joint training, making it challenging to balance the relationship between the two tasks. While dehazed images may show good dehazing performance, they are not always optimal for subsequent fusion tasks. Additionally, the two-stage process of dehazing followed by fusion involves different methodologies, reducing the model’s compactness.

To address the issues arising from the two-stage processing paradigm, Li et al. [6] proposed the all-weather multi-modality image fusion method, which achieves image restoration and fusion under various complex weather conditions. However,

this method fails to effectively coordinate the differences between the different restoration tasks, limiting further improvements in restoration and fusion performance. In response, Yi et al. [7] introduced a method called Text-IF, which guides the fusion of degraded images using semantic text. Nevertheless, this approach relies on pre-input text descriptions, increasing the complexity of model deployment. Furthermore, while Text-IF is designed for the restoration and fusion of multiple types of degraded images, it faces challenges in balancing fusion performance across various degradation scenarios without compromising individual task performance.

In response to the challenge of IR-VIS image fusion and restoration under hazy conditions, we propose an infrared-assisted joint learning framework, as shown in Fig. 1(b). To mitigate the impact of discrepancies between IR-VIS images on hazy image feature restoration, we design a prompt generation mechanism. It leverages non-shared information from input images to create a prompt selection matrix that selects and generates prompt embeddings from a prompt pool. These embeddings act as candidate features to aid in the recovery of hazy image features. For effective restoration of haze-affected features, we construct an infrared-assisted feature restoration module. It guides the selection of candidate features based on haze density to restore visible image features impacted by haze, enabling the joint processing of restoration and fusion within a single-stage framework. In this process, our focus shifts from solely enhancing the restoration of hazy visible images to emphasizing how restored features can further improve the quality of the fusion results.

To further enhance the fusion effect, we propose a multi-stage prompt embedding fusion module, which strengthens feature restoration and fusion with the help of the feature supplementation capability of the prompt generation. The proposed method not only effectively fuses IR-VIS images but also eliminates the interference of haze, producing clear and haze-free fusion results. Compared to the traditional two-stage approach of first dehazing and then fusing, our method more fully exploits the correlation between dehazing and fusion tasks, achieving a balance between them through a single-stage framework with collaborative training. Furthermore, the model structure is relatively lightweight and compact, facilitating practical deployment. Unlike existing multi-task fusion frameworks, our method is specifically designed for IR-VIS image fusion and restoration under hazy conditions, demonstrating excellent fusion and restoration performance. Therefore, our approach enriches the technical system for IR-VIS image fusion under hazy conditions and provides a new perspective for the restoration and fusion of low-quality images. In summary, the main contributions and advantages of our method are reflected in the following aspects:

- **Innovative Joint Framework.** An infrared-assisted joint learning framework for IR-VIS image fusion in hazy conditions is proposed, enabling collaborative training of dehazing and fusion tasks in a single stage. Compared to traditional two-stage methods, this framework more efficiently leverages the correlation between dehazing and fusion tasks, allowing them to complement each other and achieve a balanced outcome.

- **Prompt Generation Module and Multi-Stage Fusion.** A prompt generation module is designed to create a prompt selection matrix leveraging non-shared information to intelligently select and embed prompts that assist visible image restoration under hazy conditions. This approach not only enhances the restoration of visible image features but also minimizes the adverse impact of modality differences between IR-VIS features. Furthermore, a multi-stage feature fusion mechanism based on prompt embeddings is proposed to facilitate feature compensation and refinement, further improving the fusion result.
- **Efficient and Compact Model Structure.** The proposed method adopts a single-stage processing framework, making it more compact than the traditional two-stage dehazing and fusion approach, thereby facilitating a better balance between the two tasks. Furthermore, the method efficiently coordinates the dehazing and fusion, enabling the restored image features to more effectively support the generation of clear, haze-free, high-quality fusion results. This design not only enhances the fusion effect but also improves the model's applicability.

II. RELATED WORK

A. Typical Fusion Methods

In IR-VIS image fusion, traditional methods based on multi-scale transforms and sparse representations [9]–[13] remain relevant. However, deep learning-based techniques have become mainstream. These methods can be categorized into three types: Convolutional Neural Network (CNN)-based methods [14]–[17], hybrid CNN-Transformer methods [18]–[21], and Generative Adversarial Network (GAN)-based methods [4], [22]–[27]. CNN-based methods extract features from input images and perform fusion using specialized modules, enhancing image details and contrast. However, CNNs are limited in modeling long-range dependencies, which impacts fusion quality in complex scenes. In contrast, Transformers excel at capturing long-range dependencies but struggle with local details and edges. Hybrid methods, such as AFT [19], YDTR [20], and HitFusion [21], combine CNN with Transformer to model local and global information, improving fusion performance.

In GAN-based methods, FusionGAN [22] uses a single discriminator to fuse IR-VIS images, which does not maintain modality balance, leading to biased fusion results. To address this, subsequent research introduced dual discriminator-based GAN methods. For example, LGMGAN [23] combines a Conditional GAN with dual discriminators to fuse multi-modality information effectively. DDcGAN [24] uses dual discriminators for multi-resolution fusion, improving consistency across scales. Moreover, AttentionFGAN [27] integrates an attention mechanism to focus on important feature regions, significantly enhancing fusion performance. However, these methods assume that the images to be fused are of high quality, which makes it challenging to produce high-quality fusion results under hazy conditions.

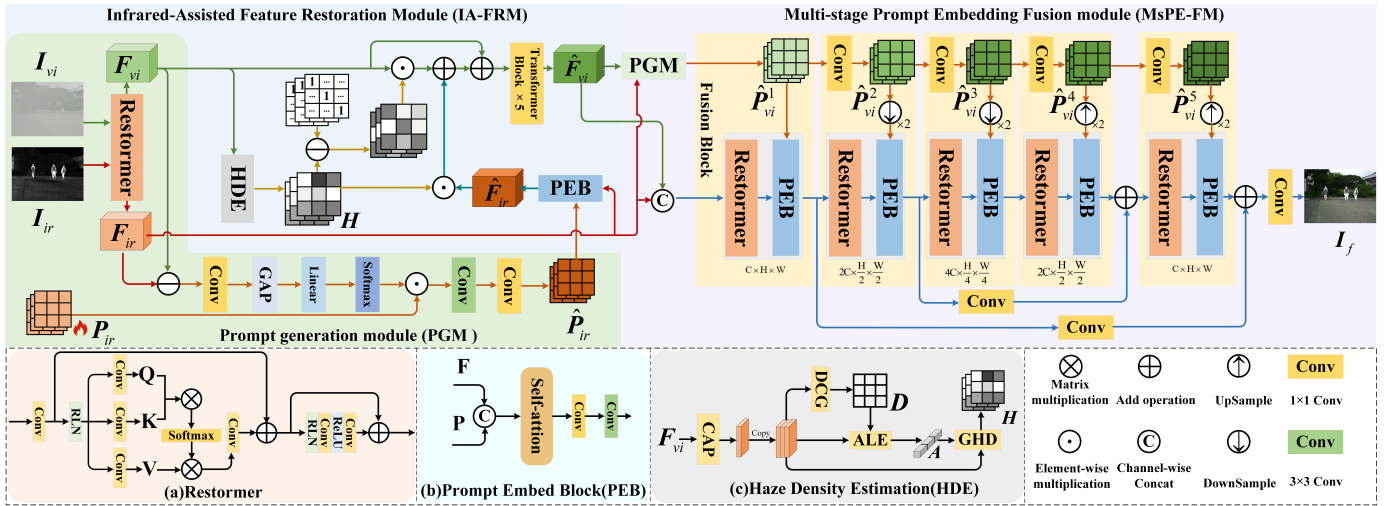


Fig. 2. Overall framework of the proposed method. The input IR and hazy VIS image pair $\{I_{ir}, I_{vi}\}$ is processed by the PGM to obtain features $\{F_{ir}, F_{vi}\}$ and a prompt \hat{P}_{ir} for F_{ir} . Through the PEB, the prompt embedding \hat{P}_{ir} is used to refine the IR feature F_{ir} , reducing redundant information and generating the refined IR feature \hat{F}_{ir} . The haze density estimation (HDE) module [8] estimates the haze density in the VIS features to dynamically adjust the proportion of injected IR information, preventing excessive IR injection. The Transformer block removes degradation from the input features to obtain haze-free features. In the MsPE-FM, the haze-free VIS features and IR features are combined and passed to the Fusion Block for feature fusion. The PGM and PEB further are used to enhance the IR-VIS complementary information, reconstructing the final fused image.

B. Methods Under Complex Imaging Conditions

Under complex imaging conditions, various factors affect the quality of visible images. Thus, achieving high-quality fusion results under these conditions has become a crucial research direction in the field of IR-VIS image fusion. In low-light conditions, PIAFusion [28] improves IR-VIS image fusion by introducing an illumination-aware loss function. DIVFusion [29] enhances dark areas, details, and reduces color distortion by separating scene illumination and enhancing texture contrast, achieving high-quality fusion in nighttime conditions. IAIFNet [30] uses an illumination enhancement network along with adaptive difference fusion and salient object awareness modules to better fuse features in IR-VIS images. LENFusion [31] generates high-contrast fusion results through three stages: brightness adjustment, enhancement, and feedback. For low-resolution images, HKD-FS [32] employs knowledge distillation to convert low-resolution IR-VIS images into high-resolution outputs. MLFusion [33] incorporates meta-learning into the IR-VIS image fusion framework, enabling fusion from inputs of any resolution to outputs of any resolution.

To address the degradation of visible images under complex conditions, a decomposition-based, interference-aware fusion method was proposed [34], which effectively fuses degraded IR-VIS images, including noisy, overexposed, and snowy images, but does not address hazy conditions. To address this, AWFusion [6] introduces a clear feature prediction module based on the atmospheric scattering model, enabling dehazing capabilities. However, AWFusion also considers other weather conditions like snow and rain, which reduces its effectiveness in hazy conditions. To balance these tasks, Text-IF [7] uses text guidance for fusion by generating modulation parameters to control cross-attention outputs, but it is not specifically designed for hazy IR-VIS fusion, resulting in suboptimal

performance. Additionally, the need for text input limits its convenience. VIFNet [35] restores hazy images using infrared images, but it focuses only on dehazing and does not address fusion. In contrast, this paper specifically focuses on IR-VIS fusion in hazy conditions to achieve clear, haze-free results.

III. THE PROPOSED METHOD

A. Overview

As shown in Fig. 2, our method comprises three core modules: the Infrared-Assisted Feature Restoration Module (IA-FRM), the Prompt Generation Module (PGM), and the Multi-stage Prompt Embedding Fusion Module (MsPE-FM). IA-FRM leverages infrared image features to assist in restoring lost information in heavily hazy regions of visible images, making it easier to restore these hazy areas. PGM generates a set of prompts to overcome the limitations of infrared images when assisting in the restoration of features in these dense hazy regions. Using the restored visible image features and prompts from PGM, MsPE-FM performs the fusion of IR-VIS image features, reconstructing a haze-free fused result.

B. Prompt Generation

Infrared imaging sensors maintain performance in hazy conditions, allowing them to penetrate heavy haze. In a rigorously registered pair of IR-VIS images $\{I_{ir}, I_{vi}\}$ provided to the model, we assume that only the visible image I_{vi} contains haze, while the infrared image I_{ir} is unaffected by haze. The core challenge of this work is to effectively utilize the infrared image I_{ir} to restore the visible image I_{vi} and then fuse them. However, the significant modality differences between IR-VIS images make it difficult to rely solely on the infrared image I_{ir} to recover the details lost in the hazy visible image. To overcome these challenges, this paper proposes the PGM,

which generates a prompt embedding to create compensatory features that address the limitations of infrared features.

As shown in Fig. 2, in the PGM, we first utilize an encoder constructed with Restormer [36] to perform feature encoding on the input registered IR-VIS images $\{I_{ir}, I_{vi}\}$. As depicted in Fig. 2(a), Restormer consists of a self-attention layer and a feed-forward network layer. The features output by the Restormer encoder are denoted as $F_{vi} \in \mathbb{R}^{C \times H \times W}$ and $F_{ir} \in \mathbb{R}^{C \times H \times W}$, where C , H , and W represent the number of channels, height, and width of the features, respectively. Additionally, in this module, the features of the hazy visible image I_{vi} and the infrared image I_{ir} are processed by:

$$F_{vi-ir} = F_{vi} - F_{ir} \quad (1)$$

to remove the shared information and highlight the unique information. The resulting difference F_{vi-ir} is then fed into a weight prediction network composed of Convolutional (Conv) layer, GAP, Linear layer, and Softmax, resulting in a weight matrix $W_p \in \mathbb{R}^{C \times H \times W}$ for selecting prompt information from the prompt pool P_{ir} . At this stage, the prompt embedding generated for compensating the infrared image features can be represented as:

$$\hat{P}_{ir} = \text{Conv}_{3 \times 3}(\text{Conv}_{1 \times 1}(W_p \odot P_{ir})) \quad (2)$$

where $P_{ir} \in \mathbb{R}^{C \times H \times W}$ is a learnable prompt pool, $\text{Conv}_{3 \times 3}$ and $\text{Conv}_{1 \times 1}$ denote 3×3 and 1×1 Conv layers, respectively. The resulting \hat{P}_{ir} is then fed, along with the infrared image features F_{ir} , into the Prompt Embedding Block (PEB) to obtain the features \hat{F}_{ir} for compensating the dense haze regions in the visible image I_{vi} .

C. Feature Restoration Assisted by Infrared Image

To effectively utilize the information provided by the infrared image I_{ir} for restoring features in haze regions, we design the IA-FRM. As shown in Fig. 2, when restoring features in hazy images, regions with higher haze density should receive more focus. Therefore, it is essential to estimate the haze density in the input images. To achieve this, we adopt the method from [8] to estimate the haze density in the input image features, as illustrated in Fig. 2(c). Specifically, the dark channel information of F_{vi} is obtained through the Dark Channel Generation (DCG) operation. The resulting dark channel information, along with the feature \tilde{F}_{vi} , is then fed into the Atmospheric Light Estimation (ALE) module to predict the atmospheric light, denoted as A . Here, \tilde{F}_{vi} is obtained by applying Channel Average Pooling (CAP) to F_{vi} , followed by channel replication. Based on A and \tilde{F}_{vi} , we can obtain the initial transmission map for each pixel location through the Get Haze Density (GHD) block, as shown in Eq. (3):

$$T = \mathbf{1} - \omega \cdot \text{DCG}(\tilde{F}_{vi} \odot A^{-1}) \quad (3)$$

where ω is a constant that adjusts the effect of the DCG prediction, set to 0.95 as suggested in [8]; $\mathbf{1} \in \mathbb{R}^{1 \times H \times W}$ is a matrix of ones; and A^{-1} represents the element-wise reciprocal of the atmospheric light A , which is broadcast along the channel dimension to match the dimension of \tilde{F}_{vi} .

Then, in the GHD block, the transmission map T is refined using a guided filter, yielding the refined transmission map T' . Since the transmission map is inversely proportional to the haze density, we estimate the haze density H through the following equation:

$$H = \mathbf{1} - T' \quad (4)$$

In H , the higher the haze density, the larger the corresponding value. Therefore, H is used to select the information for restoring F_{vi} from \hat{F}_{ir} . In this process, we use $(\mathbf{1} - H)$ to remove the information from regions with heavier haze in F_{vi} and replace it with corresponding information from \hat{F}_{ir} to assist in restoring these regions. The specific process can be formulated as:

$$\hat{F}_{vi} = TF(\hat{F}_{ir} \odot H + F_{vi} \odot (\mathbf{1} - H) + F_{vi}) \quad (5)$$

where TF denotes Transformer block. To ensure the quality of \hat{F}_{vi} , it is passed through a 3×3 Conv to obtain the dehazed image \hat{I}_{vi} , and L_1 -loss is used to optimize the network:

$$\ell_1 = \left\| \hat{I}_{vi} - I_{vi,gt} \right\|_1 \quad (6)$$

Here, $I_{vi,gt}$ represents the corresponding ground truth haze-free visible image.

D. Multi-stage Prompt Embedding Fusion

With the assistance of infrared features \hat{F}_{ir} , we obtain the dehazed visible image features \hat{F}_{vi} . These features are then fused with the infrared image features F_{ir} to reconstruct a dehazed fusion result. This approach enables us to fuse hazy IR-VIS images within a single framework, producing a dehazed fusion output. In this process, an effective fusion method is essential to achieve high-quality fusion results. To prevent residual haze in \hat{F}_{vi} from affecting the fusion, we propose the MsPE-FM.

As shown in Fig. 2, in the MsPE-FM, the restored feature \hat{F}_{vi} and the initial feature F_{ir} are input into the PGM to obtain the prompt embedding \hat{P}_{vi}^1 at the first stage of the fusion process. After concatenating \hat{F}_{vi} and F_{ir} , the result is passed through the Restormer [36]. This output, along with \hat{P}_{vi}^1 , is then input into the PEB to obtain the fusion result for the next stage. In the second stage, \hat{P}_{vi}^1 is first passed through a 1×1 Conv layer to adjust the number of channels, resulting in the adjusted prompt embedding \hat{P}_{vi}^2 , which adapts to the changes in feature channels during the second-stage feature extraction. In this fusion process, five fusion blocks, each consisting of prompt embeddings, a Restormer, and a PEB, are used to achieve the fusion of IR-VIS features. Within these fusion blocks, two residual connections are employed to prevent information loss. Finally, the fused features pass through a 1×1 Conv layer to reconstruct the fused result I_f .

To ensure that the gradients of the fusion result are consistent with those of the input infrared image and the clear visible image across the three RGB channels, we employ the gradient loss from [37] to optimize the parameters of the entire network:

$$\ell_v = \frac{1}{HW} \sum_{i=1}^3 \left\| \nabla I_f^i - \max(|\nabla I_{ir}^i|, |\nabla I_{vi,gt}^i|) \right\|_1 \quad (7)$$

where ∇ denotes the gradient operator, and i represents the R, G, B channels. Additionally, to ensure that the fused image maintains consistent pixel intensity with both the IR and VIS images, we utilize a pixel intensity consistency loss function ℓ_{int} to update the network parameters:

$$\ell_{int} = \frac{1}{HW} \sum_{i=1}^3 \|\mathbf{I}_f^i - \max(\mathbf{I}_{ir}, \mathbf{I}_{vi,gt}^i)\|_1 \quad (8)$$

The total loss is then formulated as:

$$\ell_{total} = \ell_{int} + \ell_{\nabla} + \alpha \ell_1 \quad (9)$$

where α is a hyperparameter that adjusts the contribution of the L_1 -loss in this optimization process.

IV. EXPERIMENTS

A. Experimental Configurations

Dataset. In this work, we utilize 1,083 IR-VIS image pairs from the MSRS dataset [28] as the training set. This dataset includes a wide variety of scenes, such as vehicles, pedestrians, houses, and streets, offering a rich and diverse set of visual data for training purposes. For testing, we use 361 image pairs from the MSRS dataset for both qualitative and quantitative comparative experiments, ensuring no overlap with the training set. Additionally, we assess the effectiveness and generalization capability of our method on 100 image pairs from the M³FD dataset [26] and 50 image pairs from the RoadScene dataset [38]. The M³FD dataset contains IR-VIS image pairs from scenes such as university campuses, vacation spots, and urban main roads, while the RoadScene dataset includes IR-VIS image pairs selected from the representative scenes including pedestrians, vehicles, roads, and buildings. To generate hazy image pairs, we apply the atmospheric scattering model [8] to introduce haze into the visible images in both the training and test sets.

Metrics. To objectively evaluate the fusion performance of different methods, we adopt five commonly used image quality assessment metrics: Mutual Information (Q_{MI}) [39], Gradient-based Fusion Performance ($Q_{AB/F}$) [40], Chen-Varshney Metric (Q_{CV}) [41], Sum of Correlation of Differences (Q_{SCD}) [42], and Visual Information Fidelity (Q_{VIF}) [43]. These metrics are used to assess the quality of the fusion results, with clear source images (without haze) as reference images when necessary. Additionally, to evaluate the perceptual quality of the dehazing effects within the fusion results, we employ the Perceptual Index (Q_{PI}) [44], Natural Image Quality Evaluator (Q_{NIQE}) [45], and Spatial Frequency (Q_{SF}) [46]. According to the evaluation criteria, lower Q_{CV} , Q_{PI} , and Q_{NIQE} values indicate better fusion performance, while higher values for the remaining metrics signify improved quality.

B. Implementation Details

All experiments are conducted using the PyTorch framework on a single 24GB NVIDIA GeForce RTX 4090 GPU. During training, images are randomly cropped to 256×256 patches, with data augmentation techniques such as horizontal and vertical flipping applied. The model is trained for a total of

300 epochs, using a batch size of 6 and the AdamW optimizer [47]. The initial learning rate is set to 2×10^{-4} and is gradually reduced to 2×10^{-6} following a cosine annealing schedule.

C. Comparison with State-of-the-art Methods

In order to verify the effectiveness of our method, we compare it with two existing methods. The first methodology involves initially applying advanced image dehazing algorithms to remove haze from the visible images, followed by fusing the dehazed images with the infrared images. For this purpose, we select the latest and most effective dehazing methods, namely DIACMP [48] and Dehazformer [49]. Next, we apply representative IR-VIS image fusion methods, such as MLFusion [33], U2Fusion [38], LRRNet [16], ALFusion [18], TIMFusion [50], and MRFS [51], to fuse the dehazed visible images with the infrared images. The second methodology employs the Text-IF method [7], which directly restores and fuses hazy images with the assistance of text information.

Experiments on MSRS dataset. To intuitively evaluate the fusion performance of different algorithms on the MSRS dataset, four pairs of IR-VIS images are selected, as shown in Fig. 3. As indicated from the red boxes in the first and second rows of Fig. 3, our method effectively preserves thermal radiation information, clearly highlighting the trousers of pedestrians, which most other methods fail to achieve. Although TIMFusion and Text-IF can also accomplish this to some extent, the results within the purple boxes reveal that they fail to accurately restore the texture details of trees, resulting in blurred outputs. In the red boxes of the third and fourth rows, our method preserves the details of windows while maintaining the scene brightness, producing a clear and well-restored window. In contrast, MLFusion, U2Fusion, and ALFusion suffer from brightness loss, leading to blurred scenes and poor visual effects. LRRNet, TIMFusion, MRFS, and Text-IF fail to deliver satisfactory contrast. Moreover, the other two sets of experimental results shown in Fig. 3 further highlight that the proposed method achieves superior visual performance compared to the competing methods.

Additionally, we conduct a quantitative comparison on 361 image pairs from the MSRS dataset to verify the effectiveness of our method. Tables I and II present the experimental results based on the DIACMP and Dehazformer dehazing methods, respectively. As shown in Tables I–II, our method ranks first across all eight metrics, demonstrating its outstanding performance on the MSRS dataset. The higher $Q_{AB/F}$ and Q_{CV} scores indicate that our fused images achieve superior detail clarity. Meanwhile, the best Q_{SCD} and Q_{VIF} scores suggest that our method ensures better visual consistency, closely matching the clear source images. The Q_{MI} metric reflects the shared information between the fused and source images, confirming that our approach preserves more source image information. As perceptual quality metrics, Q_{NIQE} and Q_{PI} evaluate image naturalness and perceptual quality in a no-reference manner, where lower values indicate better alignment with human visual perception. Furthermore, Q_{SF} measures the sharpness of image edges, demonstrating that our method produces haze-free fused images that are both natural and sharp.

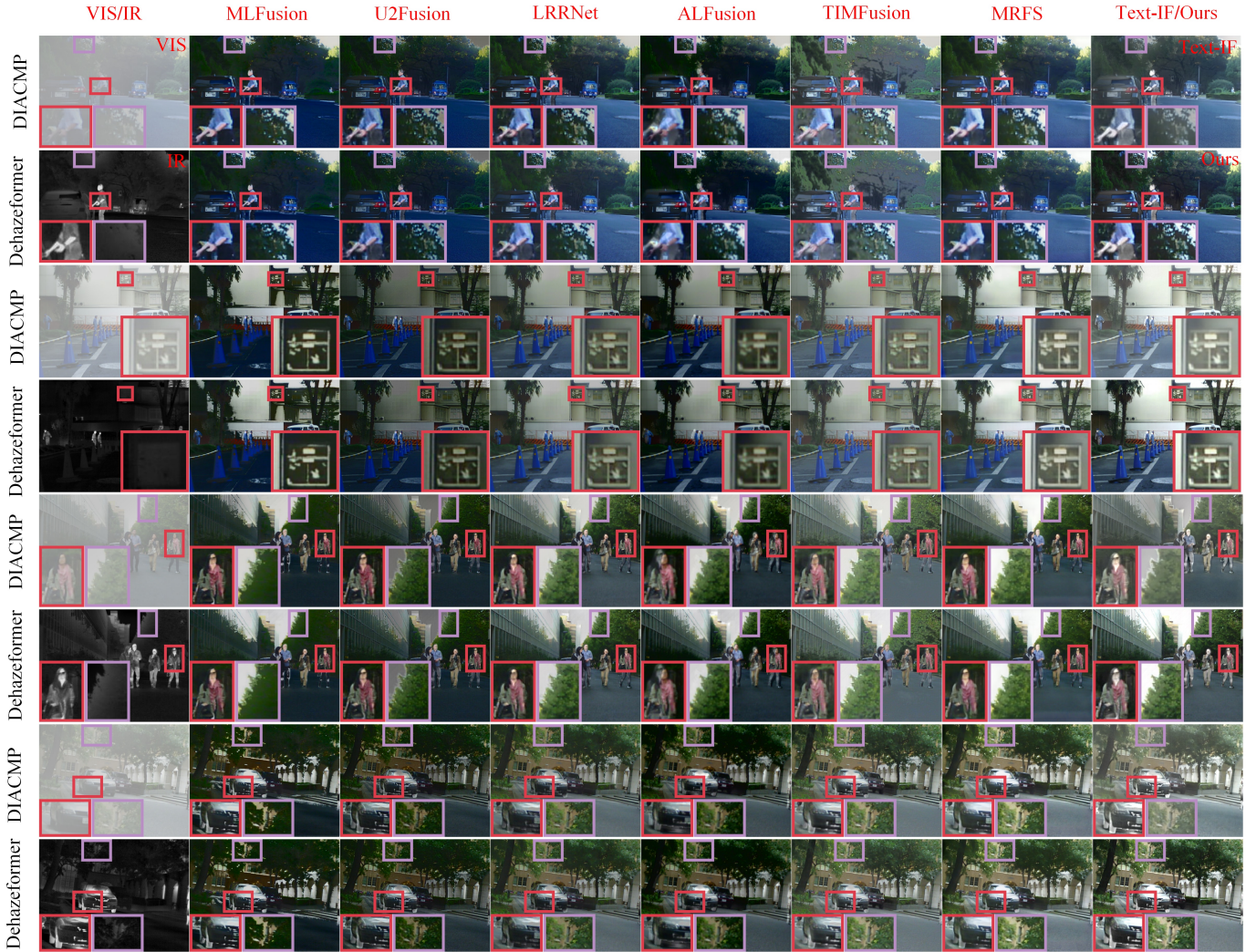


Fig. 3. Visual comparison of fusion results from different methods on the MSRS dataset. In the fusion results generated by the comparison methods, except for the last column, the first row of each image pair represents the result of first dehazing with DIACMP and then fusing. The second row shows the result of dehazing with Dehazeformer and then fusing. The last column represents the result of fusion using Text IF (first row) and our method (second row).

TABLE I
QUANTITATIVE ANALYSIS OF OUR METHOD COMPARED WITH DIACMP+FUSION AND TEXT-IF ON THE MSRS DATASET. RED INDICATES THE BEST, AND BLUE INDICATES THE SECOND BEST.

Methods	$Q_{MI} \uparrow$	$Q_{AB/F} \uparrow$	$Q_{CV} \downarrow$	$Q_{SCD} \uparrow$	$Q_{VIF} \uparrow$	$Q_{NIQE} \downarrow$	$Q_{PI} \downarrow$	$Q_{SF} \uparrow$
MLFusion	1.706	0.274	608.391	1.121	0.199	5.022	4.285	9.953
U2Fusion	1.301	0.330	838.330	1.364	0.226	4.977	4.354	7.209
LRRNet	1.864	0.441	614.101	1.000	0.288	4.750	4.333	8.479
ALFusion	1.449	0.377	700.180	1.201	0.257	5.391	5.419	7.417
TIMFusion	1.800	0.382	1048.770	1.090	0.295	4.515	4.256	8.136
MRFS	1.580	0.457	332.068	1.348	0.325	5.068	4.800	9.042
Text-IF	1.428	0.558	458.252	1.351	0.369	4.260	4.312	8.393
Ours	2.720	0.652	238.420	1.662	0.490	4.110	3.811	11.050

TABLE II
QUANTITATIVE ANALYSIS OF OUR METHOD COMPARED WITH DEHAZEFORMER+FUSION AND TEXT-IF ON THE MSRS DATASET. RED INDICATES THE BEST, AND BLUE INDICATES THE SECOND BEST.

Methods	$Q_{MI} \uparrow$	$Q_{AB/F} \uparrow$	$Q_{CV} \downarrow$	$Q_{SCD} \uparrow$	$Q_{VIF} \uparrow$	$Q_{NIQE} \downarrow$	$Q_{PI} \downarrow$	$Q_{SF} \uparrow$
MLFusion	1.720	0.270	613.291	1.119	0.199	5.052	4.337	9.826
U2Fusion	1.311	0.324	832.878	1.361	0.225	5.185	4.439	7.071
LRRNet	1.883	0.436	608.019	0.999	0.288	4.883	4.445	8.317
ALFusion	1.471	0.370	695.816	1.198	0.256	5.468	5.542	7.339
TIMFusion	1.785	0.382	1057.931	1.092	0.299	4.567	4.355	8.303
MRFS	1.603	0.448	328.901	1.340	0.323	5.150	4.905	8.843
Text-IF	1.428	0.558	458.252	1.351	0.369	4.260	4.312	8.393
Ours	2.720	0.652	238.420	1.662	0.490	4.110	3.811	11.050

Experiments on M³FD dataset. To evaluate the generalization ability of our method on the M³FD dataset, we select four pairs of IR-VIS images, with the visualization results shown in the Fig. 4. As illustrated in the first and second rows of Fig. 4, most methods exhibit blurring on the store signs, whereas

our method preserves clear edges and texture details. Although MLFusion can also retain the texture information of the signs effectively, it performs poorly in restoring background details, resulting in background blurriness. This issue is also evident in the second and third image pairs, where MLFusion and other



Fig. 4. Visual comparison of fusion results from different methods on the M³FD dataset. In the fusion results generated by the comparison methods, except for the last column, the first row of each image pair represents the result of first dehazing with DIACMP and then fusing. The second row shows the result of dehazing with Dehazeformer and then fusing. The last column represents the result of fusion using Text IF (first row) and our method (second row).

TABLE III

QUANTITATIVE ANALYSIS OF OUR METHOD COMPARED WITH DIACMP+FUSION AND TEXT-IF ON THE M³FD DATASET. RED INDICATES THE BEST, AND BLUE INDICATES THE SECOND BEST.

Methods	$Q_{MI} \uparrow$	$Q_{AB/F} \uparrow$	$Q_{CV} \downarrow$	$Q_{SCD} \uparrow$	$Q_{VIF} \uparrow$	$Q_{NIQE} \downarrow$	$Q_{PI} \downarrow$	$Q_{SF} \uparrow$
MLFusion	1.842	0.411	937.069	1.134	0.390	4.840	3.230	12.025
U2Fusion	1.607	0.511	805.163	1.266	0.358	4.908	3.377	12.009
LRRNet	1.579	0.473	724.325	1.195	0.358	4.355	3.245	11.529
ALFusion	1.510	0.419	890.521	1.205	0.322	4.878	3.960	9.291
TIMFusion	1.772	0.445	859.554	0.921	0.340	4.249	3.228	11.023
MRFS	1.756	0.514	666.466	1.208	0.415	4.304	3.277	13.071
Text-IF	1.935	0.542	634.406	1.189	0.427	5.277	3.902	11.940
Ours	2.070	0.571	640.661	1.357	0.440	4.144	3.158	14.140

TABLE IV

QUANTITATIVE ANALYSIS OF OUR METHOD COMPARED WITH DEHAZEFORMER+FUSION AND TEXT-IF ON THE M³FD DATASET. RED INDICATES THE BEST, AND BLUE INDICATES THE SECOND BEST.

Methods	$Q_{MI} \uparrow$	$Q_{AB/F} \uparrow$	$Q_{CV} \downarrow$	$Q_{SCD} \uparrow$	$Q_{VIF} \uparrow$	$Q_{NIQE} \downarrow$	$Q_{PI} \downarrow$	$Q_{SF} \uparrow$
MLFusion	1.879	0.400	1023.684	1.133	0.393	4.639	3.232	11.510
U2Fusion	1.647	0.497	824.810	1.281	0.355	5.251	3.635	11.295
LRRNet	1.592	0.463	737.595	1.206	0.360	4.528	3.455	11.116
ALFusion	1.503	0.403	922.165	1.227	0.324	5.095	4.196	8.974
TIMFusion	1.719	0.449	814.112	0.919	0.336	4.420	3.357	11.325
MRFS	1.788	0.509	693.528	1.200	0.417	4.467	3.460	12.551
Text-IF	1.935	0.542	634.406	1.189	0.427	5.277	3.902	11.940
Ours	2.070	0.571	640.661	1.357	0.440	4.144	3.158	14.140

methods display color distortion in the sky regions. Thanks to the incorporation of infrared information during the dehazing stage in our method, the network effectively restores these sky regions, achieving superior restoration and fusion results.

In terms of preserving thermal target information, our

method also demonstrates a leading performance, which is particularly evident in the results shown in the fifth and sixth rows. Methods such as U2Fusion, LRRNet, ALFusion, and TIMFusion fail to retain thermal target information, leading to fusion results that do not effectively highlight thermal targets.



Fig. 5. Visual comparison of fusion results from different methods on the RoadScene dataset. In the fusion results generated by the comparison methods, except for the last column, the first row of each image pair represents the result of first dehazing with DIACMP and then fusing. The second row shows the result of dehazing with Dehazeformer and then fusing. The last column represents the result of fusion using Text IF (first row) and our method (second row).

TABLE V

QUANTITATIVE ANALYSIS OF OUR METHOD COMPARED WITH DIACMP+FUSION AND TEXT-IF ON THE ROADSCENE DATASET. RED INDICATES THE BEST, AND BLUE INDICATES THE SECOND BEST.

Methods	$Q_{MI}\uparrow$	$Q_{AB/F}\uparrow$	$Q_{CV}\downarrow$	$Q_{SCD}\downarrow$	$Q_{VIF}\uparrow$	$Q_{NIQE}\downarrow$	$Q_{PI}\downarrow$	$Q_{SF}\uparrow$
MLFusion	2.350	0.457	509.388	1.248	0.411	3.703	3.196	12.083
U2Fusion	1.852	0.492	842.539	1.201	0.342	3.856	2.960	12.650
LRRNet	1.947	0.363	622.880	0.827	0.359	3.669	3.009	12.498
ALFusion	1.753	0.327	831.380	0.956	0.273	4.311	4.191	8.793
TIMFusion	2.349	0.356	699.810	0.881	0.425	4.484	4.241	10.307
MRFS	2.115	0.391	477.748	1.362	0.393	3.932	3.615	11.269
Text-IF	2.256	0.583	497.001	1.456	0.418	3.737	3.049	13.746
Ours	2.673	0.511	454.497	1.399	0.446	3.333	2.806	14.804

TABLE VI

QUANTITATIVE ANALYSIS OF OUR METHOD COMPARED WITH DEHAZEFORMER+FUSION AND TEXT-IF ON THE ROADSCENE DATASET. RED INDICATES THE BEST, AND BLUE INDICATES THE SECOND BEST.

Methods	$Q_{MI}\uparrow$	$Q_{AB/F}\uparrow$	$Q_{CV}\downarrow$	$Q_{SCD}\downarrow$	$Q_{VIF}\uparrow$	$Q_{NIQE}\downarrow$	$Q_{PI}\downarrow$	$Q_{SF}\uparrow$
MLFusion	2.425	0.463	509.536	1.239	0.411	3.795	3.343	11.364
U2Fusion	1.864	0.495	862.820	1.175	0.340	3.873	3.029	12.117
LRRNet	1.948	0.360	617.051	0.780	0.357	3.534	2.967	12.326
ALFusion	1.726	0.315	844.762	0.934	0.257	4.321	4.258	8.545
TIMFusion	2.359	0.354	694.572	0.869	0.415	4.457	4.268	10.099
MRFS	2.119	0.396	472.542	1.332	0.389	3.847	3.619	10.922
Text-IF	2.256	0.583	497.001	1.456	0.418	3.737	3.049	13.746
Ours	2.673	0.511	454.497	1.399	0.446	3.333	2.806	14.804

In contrast, our method adopts a multi-stage prompt information injection strategy during the fusion phase, ensuring the infrared information is well-preserved. Although MLFusion, MRFS, and Text-IF can also emphasize targets to some extent,

their performance in restoring background details remains suboptimal.

Quantitative comparison results on M³FD test set, based on the DIACMP and Dehazeformer dehazing methods, are

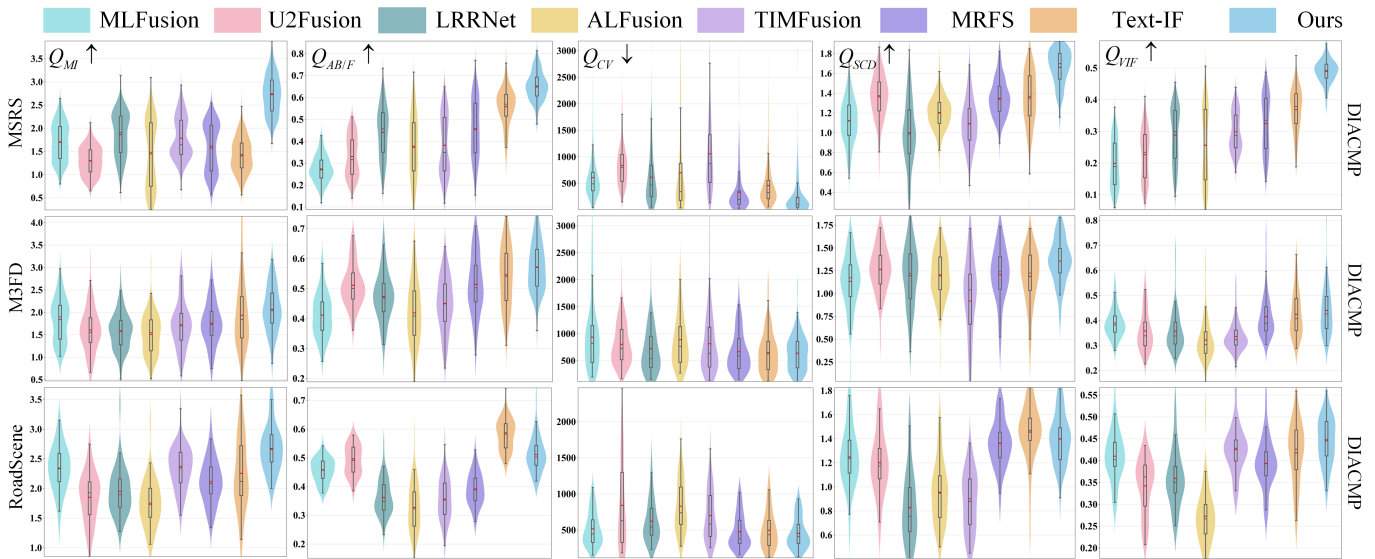


Fig. 6. Visualization of objective evaluation results. the group shows the results of using DIACMP for dehazing followed by fusion on MSRS, M³FD, and RoadScene.

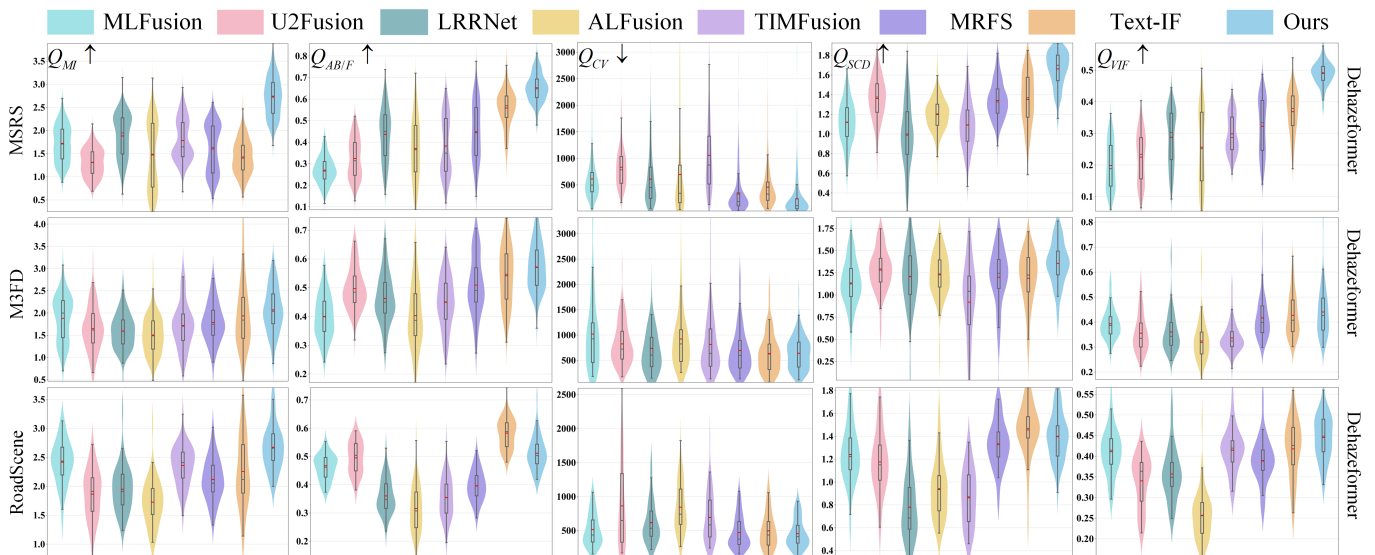


Fig. 7. Visualization of objective evaluation results. the group shows the results of using Dehazeformer for dehazing followed by fusion on MSRS, M³FD, and RoadScene.

presented in Tables III and IV, respectively. It can be observed that our proposed method ranks first in seven evaluation metrics and second in Q_{CV} , indicating its superior restoration and fusion capabilities.

Experiments on RoadScene dataset. We select four pairs of IR-VIS images from the RoadScene dataset to further evaluate the effectiveness and generalization capability of our method. The qualitative comparison results are presented in the Fig. 5. As shown in the first set of results in Fig. 5, our approach provides sharper object edges and more detailed textures. In the third and fourth rows, the content on the billboard within the red box is significantly clearer in our method compared to others, where varying degrees of blurriness are observed. Notably, the content displayed by Text-IF is completely unrecognizable. The results in the fifth

and sixth rows indicate that our method can generate fused images with high contrast, preserving the original colors of the signboards while maintaining clear edges. From the results in the red box in the seventh and eighth rows, it can be seen that our method clearly highlights the information of distant vehicles, whereas the results generated by MLFusion, MRFS, and Text-IF are relatively blurry. Although other comparison methods can somewhat enhance vehicle information, as shown in the results in the purple box, their ability to restore the distant sky and roof areas is inferior to that of our method.

Quantitative comparison results on the RoadScene dataset are presented in Tables V and VI, which utilize the DIACMP and Dehazeformer dehazing methods respectively. Our method ranks first in six evaluation metrics, with $Q_{AB/F}$ and Q_{SCD} ranking second. The best Q_{NIQE} and Q_{PI} scores indicate that

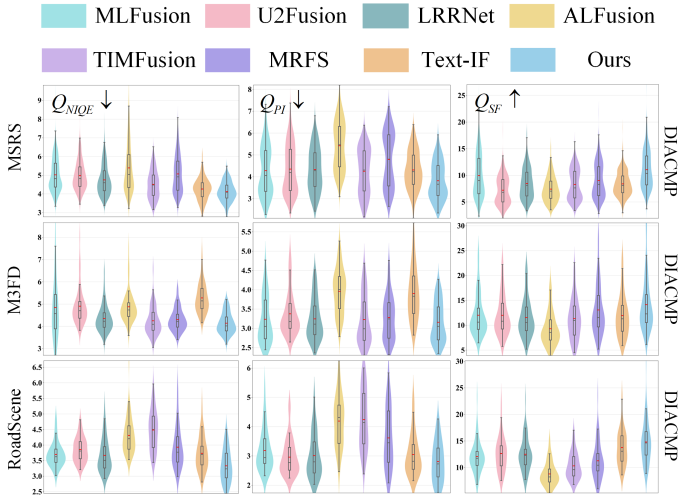


Fig. 8. Visualization of objective evaluation results. the group presents the objective evaluation results of fusion images obtained using DIACMP dehazing method, assessed with haze evaluation metrics.

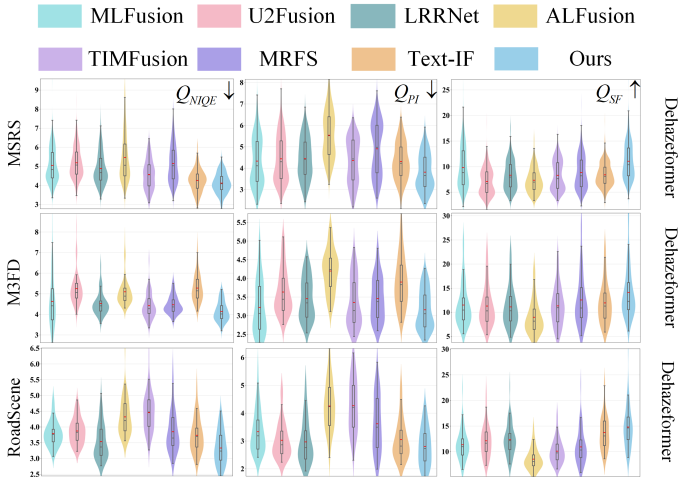


Fig. 9. Visualization of objective evaluation results. the group presents the objective evaluation results of fusion images obtained using Dehazformer dehazing method, assessed with haze evaluation metrics.

our method generates fused images that are both natural and sharp.

To further validate the advantages of our method, we present violin plots for quantitative comparison in Figs. 6–9. These plots combine data density distribution (represented by the shape of the violin) with statistical features (embedded box plots). The width of each violin reflects data density, with wider sections indicating higher concentration. The embedded box plot shows key statistics: the red horizontal line indicates the mean, the box spans the 25% to 75% data range, the black line in the middle represents the median. The vertical axis represents the metric values, with the different-colored boxes corresponding to the results obtained by the various methods. These plots allow for a clear comparison of distribution, central tendencies, and variability across methods, highlighting performance differences effectively.

We categorize the metrics into two groups reflecting fusion quality and dehazing quality, organized based on the dehazing methods used. Fig. 6 presents violin plots of fusion metrics across three datasets, comparing our method with the combination of DIACMP for dehazing followed by fusion, and the Text-IF method. As shown in the Q_{MI} metric’s violin plot, our method achieves the highest mean, with a more concentrated high-density distribution and relatively smaller variability, indicating that our data distribution is more centralized, demonstrating robust and stable performance in image fusion. Fig. 7 displays violin plots comparing our method with the combination of Dehazformer for dehazing followed by fusion, and the Text-IF method. The results clearly show that our method exhibits superior fusion performance.

Fig. 8 illustrates violin plots of dehazing metrics across three datasets, comparing our method with the combination of DIACMP for dehazing followed by fusion, and the Text-IF method. As depicted in the Q_{NIQE} metric’s violin plot, our method achieves the lowest score while showing a more concentrated distribution skewed towards lower values and exhibiting smaller variability compared to other methods. Fig. 9 shows violin plots comparing our method with the combination of Dehazformer for dehazing followed by fusion, and the Text-IF method. The violin plots for all three metrics demonstrate that our method achieves stable and outstanding performance in image restoration.

D. Ablation Study

We design six experimental settings to evaluate the effectiveness of each module. In the first setting, we remove the PGM-generated prompt \hat{P}_{ir} , the haze density estimation (HDE) module, and the process of supplementing visible features with infrared features based on haze density, directly inputting F_{vi} into the Transformer Block for dehazing (denoted as “w/o F_{ir} ”) to assess the auxiliary role of infrared information. In the second setting, we replace the operation in Eq. (5) by directly adding \hat{F}_{ir} and F_{vi} (denoted as “w/o HDE”) to validate the impact of haze-density-based infrared integration. In the third setting, we remove the prompt embedding for \hat{P}_{ir} and the PEB module, injecting infrared features extracted by the encoder, guided by haze density H , directly into F_{vi} (denoted as “w/o \hat{P}_{ir} ”) to evaluate the effect of prompt embedding. In the fourth setting, we test the effectiveness of the PEB module by removing it from IA-FRM, denoted as “w/o FR-PEB”. In the fifth setting, we remove \hat{P}_{vi} from MsPE-FM to verify the effectiveness of prompt embedding, denoted as “w/o \hat{P}_{vi} ”. In the sixth setting, we omit the PEB from the Fusion Block, performing feature concatenation and convolution directly (denoted as “w/o FB-PEB”) to validate its role in fusion.

Table VII and Fig. 10 demonstrate the impact of each module on fusion performance. While removing any module leads to performance decrease, these changes may not be readily visible in the qualitative results but are clearly reflected in the quantitative data. As shown in Table VII, when infrared information is not used to supplement visible features, the metrics Q_{PI} and Q_{NIQE} increase significantly, and all fusion

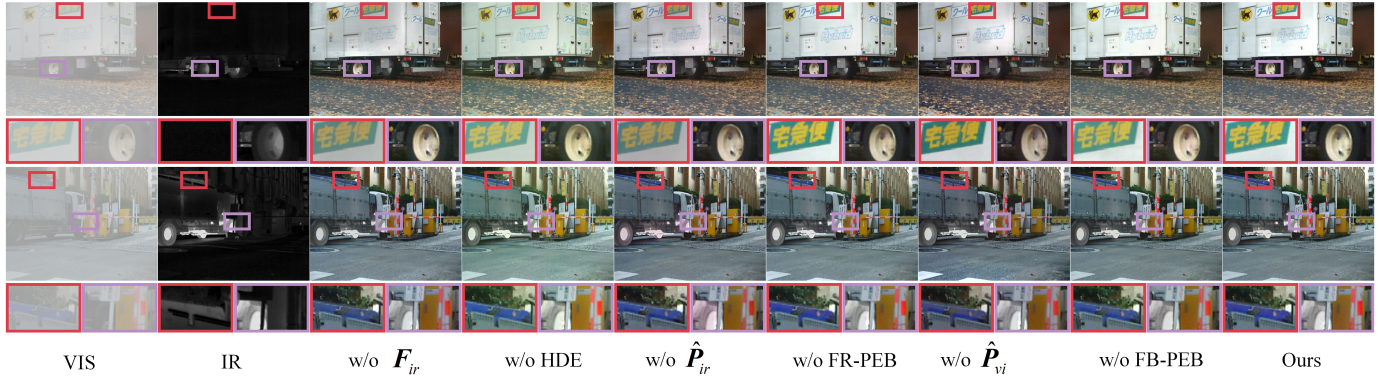


Fig. 10. Ablation study on the fusion network design. The first two columns are the input source images, and the third to ninth columns are different fusion network.

TABLE VII

QUANTITATIVE RESULTS OF SIX ABLATION EXPERIMENTS ON THE MSRS DATASET, WITH THE VALUES IN RED INDICATING THE BEST PERFORMANCE AND THOSE IN BLUE INDICATING THE SECOND-BEST.

Models	$Q_{PI} \downarrow$	$Q_{NIQE} \downarrow$	$Q_{AB/F} \uparrow$	$Q_{VIF} \uparrow$	$Q_{SCD} \uparrow$	$Q_{CV} \downarrow$	$Q_{MI} \uparrow$	$Q_{SF} \uparrow$
w/o F_{ir}	3.866	4.217	0.651	0.483	1.631	252.400	2.520	11.120
w/o HDE	3.887	4.319	0.644	0.464	1.585	253.014	2.337	10.657
w/o \hat{P}_{ir}	3.851	4.259	0.648	0.481	1.628	246.616	2.521	10.848
w/o FR-PEB	3.819	4.099	0.644	0.475	1.601	251.357	2.349	10.942
w/o \hat{P}_{vi}	3.820	4.212	0.638	0.478	1.598	294.239	2.132	10.902
w/o FB-PEB	3.846	4.115	0.645	0.481	1.656	241.963	2.607	10.854
Ours	3.811	4.110	0.652	0.490	1.662	238.420	2.720	11.050

TABLE VIII

QUANTITATIVE ANALYSIS OF SIX DIFFERENT α MODELS ON THE MSRS DATASET UNDER THE CONDITION OF $M = 5$. RED INDICATES THE BEST, AND BLUE INDICATES THE SECOND BEST.

α	$Q_{MI} \uparrow$	$Q_{AB/F} \uparrow$	$Q_{CV} \downarrow$	$Q_{SCD} \uparrow$	$Q_{VIF} \uparrow$	$Q_{NIQE} \downarrow$	$Q_{PI} \downarrow$	$Q_{SF} \uparrow$
0.5	2.711	0.650	241.934	1.646	0.489	4.211	3.816	11.115
1	2.764	0.660	239.645	1.656	0.483	4.209	3.821	11.083
2	2.720	0.652	238.420	1.662	0.490	4.110	3.811	11.050
3	2.743	0.658	243.385	1.650	0.488	4.105	3.819	11.049
4	2.787	0.656	240.587	1.657	0.489	4.149	3.838	11.054
5	2.030	0.372	387.993	1.572	0.345	5.321	5.401	7.059

TABLE IX

QUANTITATIVE ANALYSIS OF FOUR DIFFERENT M MODELS ON THE MSRS DATASET UNDER THE CONDITION OF $\alpha = 2$. RED INDICATES THE BEST, AND BLUE INDICATES THE SECOND BEST.

M	$Q_{MI} \uparrow$	$Q_{AB/F} \uparrow$	$Q_{CV} \downarrow$	$Q_{SCD} \uparrow$	$Q_{VIF} \uparrow$	$Q_{NIQE} \downarrow$	$Q_{PI} \downarrow$	$Q_{SF} \uparrow$
1	2.567	0.651	251.174	1.669	0.484	4.113	3.816	10.967
3	2.915	0.662	244.317	1.643	0.488	4.146	3.839	10.982
5	2.720	0.652	238.420	1.662	0.490	4.110	3.811	11.050
7	2.832	0.659	238.883	1.656	0.491	4.108	3.840	11.027

metrics decrease, confirming the effectiveness of incorporating infrared information to enhance visible features. If the HDE module is excluded, and infrared information is directly injected into the visible image, model performance does not improve. Instead, color distortion appears in the fusion results, and objective evaluation metrics decline to varying degrees. Similar issues are observed in the setting “w/o \hat{P}_{ir} ”. Additionally, for the settings “w/o FR-PEB”, “w/o \hat{P}_{vi} ” and “w/o FB-PEB”, the experimental results show slight degradation in detail retention, along with a decline in objective metrics, further validating the effectiveness of each module.

E. Hyperparameters Analysis

A Our method involves two key hyperparameters: α , used to balance the $L1$ -loss, and M , representing the number of Fusion Blocks in MsPE-FM. During training, they are set to 2 and 5, respectively. To validate the rationale behind these choices, we conduct a detailed analysis of their impact on the model’s performance.

The impact of α on model performance. We fix M at 5 and study the impact of different values of α within the range (0, 5] on the model performance. Table VIII presents the quantitative evaluation results of the fusion model on the MSRS dataset for various values of α . The results indicate that when α is too small, the model performance does not reach its optimal level. Similarly, when α is too large, performance declines as well. The model achieves the best overall performance when $\alpha = 2$, which validates the choice of $\alpha = 2$ in this study.

The impact of M on model performance. To analyze the impact of different values of M on the model performance, we fix α at 2 and adjust M within the range of [1, 7] to observe how the model performance changes. As shown in Table IX, the overall performance of the model improves with the number of Fusion Blocks. However, from the results for $M = 5$ and $M = 7$, it is evident that the performance gain has plateaued. Considering that increasing the number of Fusion Blocks significantly raises the model’s parameter count, we ultimately set M to 5.

F. Complexity Analysis

This paper employs a single-stage framework for hazy image fusion, which significantly reduces the model’s complexity and parameter count. To validate this advantage, we test the FLOPs and parameter count of each model and plot a bubble chart with the fusion metric $Q_{AB/F}$ to assess the model complexity. As shown in Fig. 11, our model achieves optimal performance while maintaining a low parameter count

and the lowest computational complexity, fully demonstrating its efficiency and suitability for practical deployment.

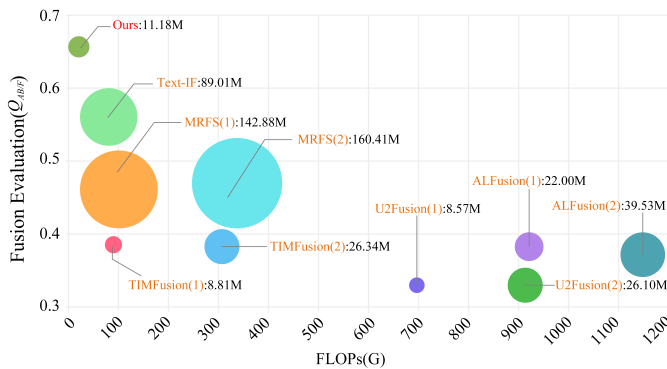


Fig. 11. Model Complexity Analysis. In the figure, the x-axis represents the FLOPs(G) for models with input images of size 256×256 , the y-axis denotes the average value of the fusion metric, and the radius of the bubbles reflects the model's parameter count. In the method names, (1) refers to the result obtained by first applying DIACMP for dehazing followed by fusion, and (2) refers to the result obtained by first applying Dehazeformer for dehazing followed by fusion.

G. Limitations and Future Work

Although our method effectively handles hazy image fusion with high quality, real-world scenarios may still present challenging weather conditions such as low light, snow, and rain. Our approach does not currently account for the impact of these factors. While some existing methods have attempted to address this issue, they fail to effectively balance the impact of different degradations on the fusion results. Furthermore, these methods typically assume that the degradation types in the images have been encountered by the model, and the model performance tends to be suboptimal in scenarios with unseen degradations. Therefore, future work will focus on designing a multi-degradation joint processing framework to enable the model to effectively perform fusion and restoration even in scenarios with unseen degradations.

V. CONCLUSION

This paper presents an infrared-assisted joint learning framework for IR-VIS image fusion under hazy conditions. By integrating dehazing and fusion tasks into a single-stage framework with collaborative training, our method effectively enhances feature restoration and fusion performance. Experimental results demonstrate that our approach produces clear, haze-free fusion images, outperforming traditional two-stage methods and existing multi-task fusion frameworks. The lightweight and compact model structure also ensures practical deployment, making it a valuable solution for hazy image restoration and fusion.

REFERENCES

[1] K. Du, H. Li, Y. Zhang, and Z. Yu, "Chitnet: A complementary to harmonious information transfer network for infrared and visible image fusion," *IEEE Transactions on Instrumentation and Measurement*, vol. 74, pp. 1–17, 2025.

[2] H. Li, Z. Yang, Y. Zhang, W. Jia, Z. Yu, and Y. Liu, "Mulfs-cap: Multimodal fusion-supervised cross-modality alignment perception for unregistered infrared-visible image fusion," *IEEE Transactions on Pattern Analysis and Machine Intelligence*, pp. 1–18, 2025.

[3] H. Bai, Z. Zhao, J. Zhang, B. Jiang, L. Deng, Y. Cui, S. Xu, and C. Zhang, "Deep unfolding multi-modal image fusion network via attribution analysis," *IEEE Transactions on Circuits and Systems for Video Technology*, pp. 1–1, 2024.

[4] H. Zhou, W. Wu, Y. Zhang, J. Ma, and H. Ling, "Semantic-supervised infrared and visible image fusion via a dual-discriminator generative adversarial network," *IEEE Transactions on Multimedia*, vol. 25, pp. 635–648, 2023.

[5] D. Rao, T. Xu, and X.-J. Wu, "Tgfuse: An infrared and visible image fusion approach based on transformer and generative adversarial network," *IEEE Transactions on Image Processing*, pp. 1–1, 2023.

[6] X. Li, W. Liu, X. Li, and H. Tan, "Physical perception network and an all-weather multi-modality benchmark for adverse weather image fusion," *arXiv preprint arXiv: 2402.02090*, 2024.

[7] X. Yi, H. Xu, H. Zhang, L. Tang, and J. Ma, "Text-if: Leveraging semantic text guidance for degradation-aware and interactive image fusion," in *Proceedings of the IEEE/CVF Conference on Computer Vision and Pattern Recognition (CVPR)*, 2024, pp. 27 026–27 035.

[8] K. He, J. Sun, and X. Tang, "Single image haze removal using dark channel prior," *IEEE Transactions on Pattern Analysis and Machine Intelligence*, vol. 33, no. 12, pp. 2341–2353, 2011.

[9] H. Li and X.-J. Wu, "Densefuse: A fusion approach to infrared and visible images," *IEEE Transactions on Image Processing*, vol. 28, no. 5, pp. 2614–2623, 2019.

[10] H. Li, X.-J. Wu, and J. Kittler, "Rfn-nest: An end-to-end residual fusion network for infrared and visible images," *Information Fusion*, vol. 73, pp. 72–86, 2021.

[11] J. Liu, X. Fan, J. Jiang, R. Liu, and Z. Luo, "Learning a deep multi-scale feature ensemble and an edge-attention guidance for image fusion," *IEEE Transactions on Circuits and Systems for Video Technology*, vol. 32, no. 1, pp. 105–119, 2022.

[12] W. Zhao, S. Xie, F. Zhao, Y. He, and H. Lu, "Metafusion: Infrared and visible image fusion via meta-feature embedding from object detection," in *Proceedings of the IEEE/CVF Conference on Computer Vision and Pattern Recognition (CVPR)*, 2023, pp. 13 955–13 965.

[13] H. Li, Y. Wang, Z. Yang, R. Wang, X. Li, and D. Tao, "Discriminative dictionary learning based multiple component decomposition for detail-preserving noisy image fusion," *IEEE Transactions on Instrumentation and Measurement*, vol. 69, no. 4, pp. 1082–1102, 2020.

[14] H. Li, J. Zhao, J. Li, Z. Yu, and G. Lu, "Feature dynamic alignment and refinement for infrared-visible image fusion: Translation robust fusion," *Information Fusion*, vol. 95, pp. 26–41, 2023.

[15] J. Liu, R. Lin, G. Wu, R. Liu, Z. Luo, and X. Fan, "Coconet: Coupled contrastive learning network with multi-level feature ensemble for multi-modality image fusion," *International Journal of Computer Vision*, vol. 132, no. 5, pp. 1748–1775, 2024.

[16] H. Li, T. Xu, X.-J. Wu, J. Lu, and J. Kittler, "Lrrnet: A novel representation learning guided fusion network for infrared and visible images," *IEEE Transactions on Pattern Analysis and Machine Intelligence*, vol. 45, no. 9, pp. 11 040–11 052, 2023.

[17] H. Li, J. Zhao, J. Li, Z. Yu, and G. Lu, "Feature dynamic alignment and refinement for infrared-visible image fusion: Translation robust fusion," *Information Fusion*, vol. 95, pp. 26–41, 2023. [Online]. Available: <https://www.sciencedirect.com/science/article/pii/S1566253523000519>

[18] H. Li, J. Liu, Y. Zhang, and Y. Liu, "A deep learning framework for infrared and visible image fusion without strict registration," *International Journal of Computer Vision*, vol. 132, p. 1625–1644, 2024.

[19] Z. Chang, Z. Feng, S. Yang, and Q. Gao, "Aft: Adaptive fusion transformer for visible and infrared images," *IEEE Transactions on Image Processing*, vol. 32, pp. 2077–2092, 2023.

[20] W. Tang, F. He, and Y. Liu, "Ydtr: Infrared and visible image fusion via y-shape dynamic transformer," *IEEE Transactions on Multimedia*, vol. 25, pp. 5413–5428, 2022.

[21] J. Chen, J. Ding, and J. Ma, "Hitfusion: Infrared and visible image fusion for high-level vision tasks using transformer," *IEEE Transactions on Multimedia*, vol. 26, pp. 10 145–10 159, 2024.

[22] J. Ma, W. Yu, P. Liang, C. Li, and J. Jiang, "Fusiongan: A generative adversarial network for infrared and visible image fusion," *Information Fusion*, vol. 48, pp. 11–26, 2019.

[23] H. Xu, P. Liang, W. Yu, J. Jiang, and J. Ma, "Learning a generative model for fusing infrared and visible images via conditional generative adversarial network with dual discriminators," in *Proceedings of the*

- Twenty-Eighth International Joint Conference on Artificial Intelligence (IJCAI)*, 2019, pp. 3954–3960.
- [24] J. Ma, H. Xu, J. Jiang, X. Mei, and X.-P. Zhang, “Ddcgan: A dual-discriminator conditional generative adversarial network for multi-resolution image fusion,” *IEEE Transactions on Image Processing*, vol. 29, pp. 4980–4995, 2020.
- [25] Y. Yang, J. Liu, S. Huang, W. Wan, W. Wen, and J. Guan, “Infrared and visible image fusion via texture conditional generative adversarial network,” *IEEE Transactions on Circuits and Systems for Video Technology*, vol. 31, no. 12, pp. 4771–4783, 2021.
- [26] J. Liu, X. Fan, Z. Huang, G. Wu, R. Liu, W. Zhong, and Z. Luo, “Target-aware dual adversarial learning and a multi-scenario multi-modality benchmark to fuse infrared and visible for object detection,” in *Proceedings of the IEEE/CVF Conference on Computer Vision and Pattern Recognition (CVPR)*, 2022, pp. 5802–5811.
- [27] J. Li, H. Huo, C. Li, R. Wang, and Q. Feng, “Attentionfgan: Infrared and visible image fusion using attention-based generative adversarial networks,” *IEEE Transactions on Multimedia*, vol. 23, pp. 1383–1396, 2021.
- [28] L. Tang, J. Yuan, H. Zhang, X. Jiang, and J. Ma, “Piafusion: A progressive infrared and visible image fusion network based on illumination aware,” *Information Fusion*, vol. 83-84, pp. 79–92, 2022.
- [29] L. Tang, X. Xiang, H. Zhang, M. Gong, and J. Ma, “Divfusion: Darkness-free infrared and visible image fusion,” *Information Fusion*, vol. 91, pp. 477–493, 2023.
- [30] Q. Yang, Y. Zhang, Z. Zhao, J. Zhang, and S. Zhang, “Iaifnet: An illumination-aware infrared and visible image fusion network,” *IEEE Signal Processing Letters*, vol. 31, pp. 1374–1378, 2024.
- [31] J. Chen, L. Yang, W. Liu, X. Tian, and J. Ma, “Lenfusion: A joint low-light enhancement and fusion network for nighttime infrared and visible image fusion,” *IEEE Transactions on Instrumentation and Measurement*, vol. 73, pp. 1–15, 2024.
- [32] W. Xiao, Y. Zhang, H. Wang, F. Li, and H. Jin, “Heterogeneous knowledge distillation for simultaneous infrared-visible image fusion and super-resolution,” *IEEE Transactions on Instrumentation and Measurement*, vol. 71, pp. 1–15, 2022.
- [33] H. Li, Y. Cen, Y. Liu, X. Chen, and Z. Yu, “Different input resolutions and arbitrary output resolution: A meta learning-based deep framework for infrared and visible image fusion,” *IEEE Transactions on Image Processing*, vol. 30, pp. 4070–4083, 2021.
- [34] X. Li, X. Li, and H. Tan, “Decomposition based and interference perception for infrared and visible image fusion in complex scenes,” *arXiv preprint arXiv: 2402.02096*, 2024.
- [35] M. Yu, T. Cui, H. Lu, and Y. Yue, “Vifnet: An end-to-end visible-infrared fusion network for image dehazing,” *Neurocomputing*, p. 128105, 2024.
- [36] S. W. Zamir, A. Arora, S. Khan, M. Hayat, F. S. Khan, and M. Yang, “Restormer: Efficient transformer for high-resolution image restoration,” in *2022 IEEE/CVF Conference on Computer Vision and Pattern Recognition (CVPR)*, 2022, pp. 5718–5729.
- [37] J. Yue, L. Fang, S. Xia, Y. Deng, and J. Ma, “Dif-fusion: Toward high color fidelity in infrared and visible image fusion with diffusion models,” *IEEE Transactions on Image Processing*, vol. 32, pp. 5705–5720, 2023.
- [38] H. Xu, J. Ma, J. Jiang, X. Guo, and H. Ling, “U2fusion: A unified unsupervised image fusion network,” *IEEE Transactions on Pattern Analysis and Machine Intelligence*, vol. 44, no. 1, pp. 502–518, 2022.
- [39] G. Qu, D. Zhang, and P. Yan, “Information measure for performance of image fusion,” *Electronics Letters*, vol. 38, no. 7, p. 1, 2002.
- [40] C. S. Xydeas, V. Petrovic *et al.*, “Objective image fusion performance measure,” *Electronics Letters*, vol. 36, no. 4, pp. 308–309, 2000.
- [41] H. Chen and P. K. Varshney, “A human perception inspired quality metric for image fusion based on regional information,” *Information Fusion*, vol. 8, no. 2, pp. 193–207, 2007.
- [42] V. Aslantas and E. Bendes, “A new image quality metric for image fusion: The sum of the correlations of differences,” *Aeu-International Journal of Electronics and Communications*, vol. 69, no. 12, pp. 1890–1896, 2015.
- [43] Y. Han, Y. Cai, Y. Cao, and X. Xu, “A new image fusion performance metric based on visual information fidelity,” *Information Fusion*, vol. 14, no. 2, pp. 127–135, 2013.
- [44] Y. Blau, R. Mechrez, R. Timofte, T. Michaeli, and L. Zelnik-Manor, “The 2018 pirm challenge on perceptual image super-resolution,” in *Proceedings of the European Conference on Computer Vision Workshops (ECCVW)*, 2018, pp. 334–355.
- [45] A. Mittal, R. Soundararajan, and A. C. Bovik, “Making a “completely blind” image quality analyzer,” *IEEE Signal Processing Letters*, vol. 20, no. 3, pp. 209–212, 2013.
- [46] A. M. Eskicioglu and P. S. Fisher, “Image quality measures and their performance,” *IEEE Transactions on Communications*, vol. 43, no. 12, pp. 2959–2965, 1995.
- [47] D. P. Kingma and J. Ba, “Adam: A method for stochastic optimization,” in *International Conference on Learning Representations (ICLR)*, 2015.
- [48] Y. Zhang, S. Zhou, and H. Li, “Depth information assisted collaborative mutual promotion network for single image dehazing,” in *Proceedings of the IEEE/CVF Conference on Computer Vision and Pattern Recognition (CVPR)*, 2024, pp. 2846–2855.
- [49] Y. Song, Z. He, H. Qian, and X. Du, “Vision transformers for single image dehazing,” *IEEE Transactions on Image Processing*, vol. 32, pp. 1927–1941, 2023.
- [50] R. Liu, Z. Liu, J. Liu, X. Fan, and Z. Luo, “A task-guided, implicitly-searched and metainitialized deep model for image fusion,” *IEEE Transactions on Pattern Analysis and Machine Intelligence*, vol. 46, no. 10, pp. 6594–6609, 2024.
- [51] H. Zhang, X. Zuo, J. Jiang, C. Guo, and J. Ma, “Mrfs: Mutually reinforcing image fusion and segmentation,” in *Proceedings of the IEEE/CVF Conference on Computer Vision and Pattern Recognition (CVPR)*, 2024, pp. 26974–26983.